

Continuously tunable dipolar exciton geometry for controlling bosonic quantum phase transitions

Authors: Zhenyu Sun¹, Haoteng Sun¹, Xiaohang Jia¹, An Li¹, Naiyuan J. Zhang², Ken Seungmin Hong¹, Joseph DePinho³, Conor Y. Long⁴, Kenji Watanabe⁵, Takashi Taniguchi⁶, Ou Chen¹, Jue Wang⁷, Jia Li⁸, Brenda Rubenstein^{1,9}, and Yusong Bai^{1*}

Affiliations:

¹ Department of Chemistry, Brown University, Providence, RI, USA

² Department of Physics, University of Washington, Seattle, WA, USA

³ School of Engineering, Brown University, Providence, RI, USA

⁴ Department of Chemical and Biological Engineering, Princeton University, Princeton, NJ, USA

⁵ Research Center for Electronic and Optical Materials, National Institute for Materials Science, Namiki, Tsukuba, Japan

⁶ Research Center for Materials Nanoarchitectonics, National Institute for Materials Science, Namiki, Tsukuba, Japan

⁷ Department of Physics, The Hong Kong University of Science and Technology, Hong Kong, China

⁸ Department of Physics, University of Texas at Austin, TX, USA

⁹ Department of Physics, Brown University, Providence, RI, USA

*Corresponding author. Email: yusong_bai@brown.edu

ABSTRACT. The geometry and binding energy of excitons, set by electron-hole wavefunction distributions, are fundamental factors that underpin their many-body interactions and determine optoelectronic properties of semiconductors. However, in typical solid-state systems, these quantities are fixed by material composition and structure. Here we introduce a polarizable interlayer exciton hosted in a two-dimensional tetralayer heterostructure whose dipole length, in-plane radius, and binding energy can be continuously programmed *in situ* over a wide range, enabling direct control over the nature of excitonic many-body phase transitions. An out-of-plane electric field redistributes layer-hybridized electron-hole wavefunctions, realizing *in situ* control of exciton geometry through a strong quadratic Stark response. This tunability further regulates the nature of interaction-driven Mott transition, transforming it from gradual to abrupt. Our results establish exciton geometry as a continuously tunable materials parameter, opening routes to exciton-based quantum phase-transition simulators and guiding the design of emergent optoelectronic functionalities from programmable excitonic materials.

Excitons, Coulomb-coupled electron-hole pairs, are elementary excitations in semiconductors that play a critical role in light-matter interactions and underpin a wide range of optoelectronic applications¹⁻³. As neutral bosonic quasiparticles, they also offer an effective platform for exploring quantum many-body states⁴⁻⁸. In this context, exciton geometry, defined by the dipole moment and in-plane spatial extent of the electron-hole wavefunction, emerges as a fundamental parameter, as it governs binding energies,² optical transitions,¹ and the strength and nature of interparticle interactions.⁶⁻⁸ Seminal examples include the crossover between Bose-Einstein condensation (BEC) and the Bardeen-Cooper-Schrieffer (BCS) state^{6,9}, which is induced by continuous variations of the Coulomb pairing strength and the size of the quasiparticles.

In recent years, optically addressable interlayer excitons (IXs) in two-dimensional (2D) semiconductor heterostructures have emerged as a promising bosonic testbed for exploring new excitonic phases and interaction-driven phase transitions, owing to their long lifetimes and enhanced interparticle interactions^{4,5,10-12}. Because IXs consist of electron and hole wavefunctions largely localized in separate layers, the van der Waals stacking order and layer number introduce new degrees of freedom for tailoring exciton configurations. Examples range from dipolar excitons in twisted black phosphorus homostructures¹³, where the dipole orientation can be selected via light polarization, to quadrupolar excitons assisted by every-other-layer quantum tunnelling¹⁴⁻¹⁹. While these studies have explored discrete tunability of exciton configurations, the continuous, *in situ* control over exciton dipole moment and spatial extent has remained experimentally inaccessible in semiconducting 2D materials. To date, such control has only been achieved in graphene double-layer systems under strong magnetic fields,^{6,20} where Landau orbital wavefunctions of Coulomb-coupled electron-hole pairs can be adjusted, a mechanism not readily accessible in 2D semiconductors hosting optically addressable excitons.

Here we introduce a continuously tunable dipolar exciton with broadly adjustable sizes and binding energies formed in a tetralayer transition-metal dichalcogenide (TMD) heterostructure comprising a pair of valley-aligned homobilayers. In this system, an external electric field gradually redistributes the layer-hybridized electron and hole wavefunctions, simultaneously modulating the IX dipole length, in-plane radius, and binding energy *in situ*. This geometric tunability, manifested by a pronounced quadratic Stark response, yields large polarizability, allowing the IX static dipole moment to be varied nearly threefold. By tuning the IX geometry at fixed density, we access a previously unexplored regime in which the nature of inter-exciton interactions becomes continuously adjustable. As the dipole elongates and the in-plane radius expands, we observe a tunable quantum phase transition: the exciton Mott transition evolves from gradual to abrupt. In this way, we further address the long-standing puzzle regarding the intrinsic nature of density-driven exciton Mott transition. Together, these results establish exciton geometry, and its field-driven tunability, as a continuous control knob for bosonic many-body phase transitions, thereby opening routes to quantum-phase simulators based on dipolar excitons.

Nonlinear Stark shift and highly polarizable interlayer excitons

We fabricate dual-gate, type-II-aligned TMD heterostructures consisting of an R-stacked bilayer WSe₂ (R2L-WSe₂) on top of an R-stacked bilayer WS₂ (R2L-WS₂) (**Fig. 1a**). All adjacent layers in this tetralayer structure (R2L-WSe₂/R2L-WS₂) are aligned in the R-stacking configuration with small twist angles (~ 1 to 2°). We employ few-layer graphite to construct the dual-gate structure, where an out-of-plane electric field ($\vec{E}_z = E_z \hat{z}$) can be applied (see methods for fabrication details). In R2L-WSe₂/R2L-WS₂, we expect to observe optically generated IXs exhibiting polarizability, i.e., continuously tunable IX dipoles under an E_z (**Fig. 1b**). As we establish below, the tunability arises from layer-hybridized electron and hole wavefunctions residing at the WS₂ conduction-band minimum (CBM) and WSe₂ valence-band maximum (VBM), which can be polarized by an electric field. This field-driven wavefunction redistribution modifies both the dipole length and in-plane extent of the IX, yielding a continuously tunable exciton geometry and binding energy (*vide infra*). This controllability provides a powerful means to manipulate excitonic many-body interactions.

The quadratic Stark shift of the exciton energy under E_z directly reflects the continuously varying exciton dipole moment, i.e., its polarizability^{21,22}. The IX PL in a conventional WSe₂/WS₂ hetero-bilayer exhibits a common linear Stark shift (**Fig. 1c**), consistent with a rigid dipole moment. In contrast, we observe a pronounced nonlinear Stark shift in the E_z -dependent IX PL spectra of the tetralayer heterostructure, indicating the presence of exciton polarizability (**Fig. 1d**). We emphasize that, this observed nonlinear Stark shift consistently evince across the overall sample area (**Fig. S1**), highlighting the homogeneity of the tetralayer heterostructure sample.

We now quantify the characteristic E_z -tuning of IX dipole moment in the heterostructures. For the hetero-bilayer, the data fits the linear Stark formula $\Delta E_{IX} = -e\vec{d} \cdot \vec{E}_z$ (**Fig. 1c**, gray solid line), where ΔE_{IX} is the peak energy shift, and $e\vec{d}$ denotes dipole moment. The fitting yields a dipole moment of ~ 0.61 e nm (**Fig. 1c**, yellow solid line), consistent with the typical TMD hetero-bilayer spacing¹¹. In the tetralayer device, however, a rigid dipole does not capture the full field dependence, and a piecewise model is required to fit the Stark shift. For $E_z > 28$ mV nm⁻¹, the Stark shift again fits a linear model with a dipole moment of 0.57 e nm (**Fig. 1d**, gray and yellow solid lines), suggesting an electron-hole pair localized at the central WSe₂/WS₂ interface. For -120 mV nm⁻¹ $< E_z < 28$ mV nm⁻¹, the data is described by a second-order Stark formula: $\Delta E_{IX} = -e\vec{d}_0 \cdot \vec{E}_z - \frac{1}{2}\alpha E_z^2$, where α defines the IX polarizability and $e\vec{d}_0$ denotes the dipole moment at zero electric field. From this fit (**Fig. 1d**, gray dash line; also see SI text for details), we extract an exciton polarizability of ~ 6.8 eV nm² V⁻², among the highest value observed for 2D dipolar excitons^{22,23}. This large polarizability enables continuous tuning of the IX dipole moment over a wide range (**Fig. 1d**,

yellow dash line). At $E_z = -120$ mV nm $^{-1}$, the dipole moment of 1.54 e nm is the largest value reported in TMD heterostructures^{12,24-28}. The effective dipole can be parked anywhere from 0.57 to 1.54 e nm via an applied \vec{E}_z , distinguishing this R-stacked tetralayer system as a highly tunable low-dimensional platform for probing exciton-exciton interactions.

Origins of IX polarizability

The large IX polarizability in the R-stacked tetralayer system originates from layer-hybridized electron and hole wavefunctions in the homo-bilayer WS₂ and WSe₂, respectively. **Fig. 2a, b** show the \vec{E}_z -dependent reflectance-contrast (RC) spectra of R2L-WSe₂/R2L-WS₂, focusing on the WSe₂ (**Fig. 2a**) and WS₂ (**Fig. 2b**) A-exciton (X_A) spectral windows. In both cases, two oppositely shifting, linearly dispersing RC features are observed, crossing at $E_z = 0$ V nm $^{-1}$. Fitting these dispersions yields dipole moments of ~ 0.60 e nm (**Fig. S4**), confirming their assignment as interlayer exciton transitions in the homo-bilayers (IX_{Homo}). Crucially, these field-dependent IX_{Homo} features intersect the intralayer X_A resonances and produce avoided crossings, indicating hybridization between interlayer and intralayer excitons (schematic in **Fig. S3**). This behavior suggests X_A and IX_{Homo} mix via spatially overlapping wavefunctions arising from layer-hybridized conduction- and valence-band states^{29,30}. By fitting the avoided crossing spectral features, the hybridization energies are extracted to be ~ 11 meV for R2L-WSe₂ and ~ 8 meV for R2L-WS₂ (see SI). Notably, the absence of avoided crossings in the R-stacked WSe₂/WS₂ hetero-bilayer (**Fig. S5**) confirms that the observed hybridizations in R2L-WSe₂/R2L-WS₂ originates within each R-stacked homo-bilayer. Consistently, the extracted zero-field IX dipole moment of ~ 0.75 e nm (**Fig. 1d**) in R2L-WSe₂/R2L-WS₂ exceeds the bilayer spacing (~ 0.60 e nm), indicating intrinsic electron-hole delocalization and an extended exciton dipole even without an applied field.

Layer hybridization in the R-stacked homo-bilayers is enabled by spin-conserved band alignment at the K-K valleys. Band structure calculations show that both the CBM and VBM reside at the K-K points in R2L-WSe₂ and R2L-WS₂ (**Fig. S7**). Corresponding DFT calculations (**Fig. 2c**) reveal pronounced layer hybridization at both band edges. The wavefunction layer partitions indicate that the hybridization is stronger in R2L-WSe₂ than in R2L-WS₂ as shown in **Fig. 2c** (left two columns), which is consistent with the hybridization energies extracted from the avoided crossings in **Fig. 2a, b**.

As a control, we study a tetralayer composed of H-stacked natural bilayers (H2L-WSe₂/H2L-WS₂), where opposite valley spin orientations at K-K prohibit interlayer hybridization in the homobilayers³¹. DFT calculations confirm that both the CBM and VBM wavefunctions remain layer-localized (**Fig. 2c**, right two columns). Consistently, the E_z -dependent RC spectra show no avoided crossings (**Fig. S6**), indicating the absence of layer-hybridized electronic states. Furthermore, the E_z -dependent PL spectra exhibit piecewise-linear Stark shifts (**Fig. 2d**), corroborating electric-field-driven switching between discrete dipolar exciton

configurations rather than continuous dipole tuning. As shown in **Fig. 2d**, for $E_z > -61 \text{ mV nm}^{-1}$, the Stark shift is captured by a fixed dipole moment of $0.60 e \text{ nm}$, while for $E_z < -61 \text{ mV nm}^{-1}$ a second linear regime emerges with a dipole moment of $\sim 1.2 e \text{ nm}$, comparable to the TMD trilayer spacing (see SI for detailed analysis). The abrupt transition between these two regimes highlights the absence of continuously tunable dipole moments in the H-stacked control and directly contrasts with the smooth dipole tunability enabled by valley-spin-allowed hybridization in R2L-WSe₂/R2L-WS₂.

Electric-field control of IX radius and geometry-driven gradual-to-abrupt Mott crossover

In 2D systems, the exciton Mott transition provides an effective means to estimate the exciton in-plane radius and probe the nature of exciton-exciton interactions^{11,32,33}. We extract exciton in-plane Bohr radius using the 2D Mott criterion $1/\pi \sim n_{Mott} a_B$ ^{11,34}, which relates the critical exciton ionization density n_{Mott} to exciton Bohr radius a_B . A key spectroscopic signature of the exciton Mott transition is the excitation-density (n_{eh}) dependence of the PL linewidth broadening^{11,32,33,35}. We therefore examine n_{eh} -dependent PL spectra of IXs while tuning their dipole moment with an out-of-plane field E_z .

We thoroughly examine CW n_{eh} -dependent peak-normalized PL spectra of the R2L-WSe₂/R2L-WS₂ heterostructure over E_z ranging from 45 mV nm^{-1} to -85 mV nm^{-1} , corresponding to IX dipole moments varying from 0.57 to $1.32 e \text{ nm}$ (**Fig. S10, S11**). **Fig. 3a-c** display such results at three representative fields ($E_z = 30, 0, \text{ and } -53 \text{ mV nm}^{-1}$). The n_{eh} spans $1.2 \times 10^{10} \text{ cm}^{-2}$ to $6.8 \times 10^{12} \text{ cm}^{-2}$. Densities are calibrated by relating CW and pulsed excitation conditions (see SI Text and **Fig. S9**) following established protocols⁵. **Fig. 3d** shows the constructed full-width-at-half-maximum (FWHM) map across E_z and n_{eh} : at the lowest n_{eh} , the IX linewidth remains uniformly narrow across all E_z , with a FWHM of $\sim 10 \text{ meV}$, whereas the linewidth increases by a factor of about four to six with increasing n_{eh} (depending on E_z), verifying exciton ionization^{11,33}. We emphasize that, unlike bilayer systems, the R2L-WSe₂/R2L-WS₂ heterostructures exhibit a flat-land morphology with no discernible moiré features, as evidenced by the PFM image and the smooth, doping-dependent evolution of the RC spectra (**Fig. S12**). This unique feature makes the system an ideal platform for investigating IX-IX interactions without complications from moiré potential traps.

The exciton in-plane radius grows with increasing IX out-of-plane dipole moment. The density-driven linewidth evolution in **Fig. 3d** is quantitatively captured by an S-shaped logistic function (see SI Text and **Fig. S14, S15**), which yields the Mott density n_{Mott} and the transition width Δn_{eh} (**Fig. 3e** and **Table S1**). As summarized in **Fig. 3e**, n_{Mott} progressively shifts toward the lower excitation-density regime as the electric field is swept from positive to negative. The progressive field-driven decrease of n_{Mott} allows us to determine an expansion of the IX in-plane radius a_B using the 2D Mott criterion $1/\pi \sim n_{Mott} a_B$. Additionally, the corresponding IX binding energy E_b can be estimated from the relation $E_b \propto \hbar^2/2M_r a_B^{2.8}$, where M_r is the reduced mass. **Fig. 3f** shows variations of a_B and E_b as functions of the out-of-plane field

E_z and the static IX dipole moment $e\vec{d}$: increasing $|E_z|$ continuously enlarges $|e\vec{d}|$ and expands the in-plane a_B from ~ 3 nm to ~ 12 nm, accompanied by a monotonic decrease of the effective binding energy to ~ 6 % of that of a regular bilayer IX. The observed modulations of E_b and a_B upon tuning the IX dipole moment are highly consistent with previous theoretical predictions⁸. Additionally, steady-state pump-probe spectroscopy reveals a pronounced plasma-gain feature^{11,36} at densities closely matching n_{Mott} extracted from PL linewidth broadening (SI Text and **Fig. S18**). This correspondence confirms that the explored density regime spans the Mott transition and validates PL linewidth as a reliable signature of exciton ionization.

We observe an IX-geometry-driven gradual-to-abrupt Mott crossover, underscoring that exciton geometry governs the nature of exciton-exciton interactions. As highlighted in **Fig. 3e** (and **Table S1**), the transition width Δn_{Mott} (the density span over which Mott ionization occurs), obtained from logistic fitting (SI Text and **Fig. S14, S15**), systematically narrows with increasing dipole moment and radius. This affirms that large IXs undergo a more abrupt interaction-driven Mott ionization and demonstrates a geometry-driven gradual-to-abrupt Mott crossover that is continuously tunable by the applied field. Accordingly, the $\partial FWHM / \partial n_{eh}$ map (**Fig. S16**) reveals a clear boundary for $E_z < -40$ mV nm⁻¹. Likewise, the 30, 40, and 50 meV linewidth contours in **Fig. 3d** converge as E_z is tuned negative, revealing that the density required to reach a given linewidth decreases as the IX geometry expands. At the largest dipole moment and radius ($|e\vec{d}| \approx 1.30$ e nm, $a_B \approx 12$ nm), these contours begin merging, indicating an abrupt density-driven linewidth increase.

Notably, our observations also address a long-standing question concerning the intrinsic nature of the density-driven exciton Mott transition. Experimentally, this transition has been reported to evolve either gradually with increasing density^{35,37} or to occur abruptly as an exciton collapse^{32,38}, leaving unresolved whether the transition is intrinsically gradual or abrupt. The observed IX geometry-driven gradual-to-abrupt Mott crossover reconciles these prior discrepancies and identifies exciton geometry and binding energy as relevant parameters affecting the nature of this many-body process. The gradual-to-abrupt evolution is not observed in the E_z - n_{eh} -FWHM map of WSe₂/WS₂ hetero-bilayer (**Fig. S13**), highlighting the essential role of field-programmable IX geometry and binding energy in shaping IX-IX interactions.

Complementary evidence for the essential role of IX geometry in steering IX-IX interactions is the E_z -driven Mott transition. At low density ($\sim 4.5 \times 10^{10}$ cm⁻²), the PL linewidth remains narrow and nearly constant across the examined field range (**Fig. 3g** and **Fig. S19a**), indicating a bound IX regime; the E_z -dependent PL peak energy also follows the IX nonlinear Stark shift (**Fig. 1d**). At intermediate density ($\sim 1.5 \times 10^{12}$ cm⁻²), however, driving E_z negative induces linewidth broadening: the IX peak evolves into a ~ 70 meV-wide featureless band (**Fig. 3g** and **Fig. S19b**), characteristic of plasma-like recombination from

continuum. Concurrently, the PL peak deviates from the nonlinear Stark trajectory and bends to higher energy, indicating field-driven exciton ionization. As the IX geometry is modulated with more negative E_z , a growing fraction of excitons dissociates into free carriers. Once ionized, these carriers screen the external field, causing the Stark nonlinearity to collapse; the system behaves as a charged capacitor rather than a gas of dipoles, and well-defined excitonic dipole moments no longer exist. Importantly, because n_{eh} is calibrated to remain constant across the E_z sweep (Fig. S9), this transition is purely field-driven. Together, these observations demonstrate that the excitonic phase can be tuned not only by density but also by field-programmed IX geometry and binding energy.

Microscopic view of tunable exciton-exciton interactions

We now discuss the microscopic origins of the tunable IX-IX interactions evinced in the Mott transition. The distinct geometry of IXs and the contrasting nature of IX-IX interactions are schematically illustrated in Fig. 4a. The continuous reduction of IX binding energy plays a key role in regulating the evolution from a gradual to an abrupt Mott transition. When IXs are strongly bound, the large E_b provides an energetic buffer that stabilizes the excitonic state: as density increases, Coulomb screening continuously weakens E_b , but the large initial E_b ensures that ionization proceeds continuously along the n_{eh} axis. By contrast, when IXs are weakly bound, the bound state lies close to the continuum, and even a modest enhancement of screening can collapse E_b . Once a few excitons ionize, the resulting free carriers enhance screening further, accelerating ionization and establishing a runaway feedback loop^{33,34}. The smaller the E_b , the lower the barrier protecting the bound state and the easier it becomes for this feedback to trigger a collective, avalanche-like transition. Consistently, in the R2L-WSe₂/R2L-WS₂ heterostructure, the PL evolution transforms from a slow, gradual shift at small dipole moments to an abrupt ionization at large dipole moments. This observation aligns with previous theoretical suggestions that reducing E_b promotes the screening feedback that converts a gradual crossover into an abrupt Mott-like transition³⁹.

The increased IX radius itself can provide an additional key mechanism contributing to the observed abruptness through exchange repulsion. Based on the $E_z - n_{eh}$ – FWHM map in Fig. 3d, we identify a dilute excitation-density range $n_{eh} < 2 \times 10^{11} \text{ cm}^{-2}$, where the excitonic phase dominates. We then map the optical stiffness, $\partial E_{PL} / \partial n_{eh}$ (i.e., the optical energy penalty for adding IXs to the system), as a function of E_z and n_{eh} (Fig. 4b). Importantly, in this dilute regime, large-size IXs (e.g., $E_z < -50 \text{ mV nm}^{-1}$) exhibit stiffness roughly an order of magnitude higher than small-size IXs ($E_z > 0 \text{ mV nm}^{-1}$) (also see Fig. S20). Such a contrasting optical stiffness cannot be explained by classical dipole-dipole repulsion alone ($\propto 4\pi n_{eh} e^2 d_{IX} / \epsilon$)⁴⁰, since the dipole length differs by only a factor of two between these field regimes (see SI Text). Moreover, the consistently narrow PL linewidths and well-defined nonlinear Stark trajectories (Figs. 3g and S19) in this density range exclude ionization and band-gap-renormalization effects as possible

sources of the large $\partial E_{PL} / \partial n_{eh}$. Given the pronounced in-plane Bohr-radius extension under negative fields (**Fig. 3f**), the excess stiffness likely reflects a wavefunction-overlap-driven interaction that strengthens with exciton size. As the in-plane radius expands, the overlap between electron (and hole) envelopes belonging to different excitons increases during dynamic scattering, enhancing Pauli exchange repulsion^{41,42}. Upon ionization into the plasma phase, the system can relieve this exchange penalty associated with the large IX radius by forming a free-carrier fluid with weaker interactions. We emphasize that the role of IX wavefunction delocalization and enhanced exchange repulsion deserves further theoretical investigation to elucidate its quantitative impact on the abruptness of the interaction-driven Mott transition.

Fig. 4c places our electrically tunable IX geometry in the context of previously demonstrated platforms. Previous studies in TMD bilayers, TMD multilayers, and double-graphene heterostructures have achieved either modest variations in exciton dipole moment or access to excitons with relatively large in-plane radii, but the two degrees of freedom have remained largely decoupled and limited in range. The tetralayer system here enables a continuous and simultaneous tuning of both the IX dipole moment and the in-plane radius over a substantially broader parameter space. The accessible $|e\vec{d}|$ values span nearly a factor of three, while the Bohr radius a_B expands fourfold, reaching ~ 12 nm. This combined tunability of vertical dipole length and lateral spatial extent establishes a new regime of exciton engineering, providing a programmable geometry that directly enables the control of many-body phenomena.

Conclusion and outlook

This work establishes a new interlayer-exciton platform whose geometry (i.e., dipole moment and in-plane radius) and binding energy can be continuously programmed by an external electric field. By reshaping the excitonic wavefunction *in situ*, we gain direct control over exciton-exciton interactions, accessing regimes that are fundamentally inaccessible in systems with fixed exciton properties. Using the exciton Mott transition as a diagnostic, we show that expanding exciton geometry qualitatively alters the many-body behavior, transforming the transition from gradual to abrupt. More broadly, electric-field programmability of IX geometry enables continuous traversal of the exciton phase diagram along density and geometry axes, providing a direct route to exploring correlated excitonic phases, including dipolar crystals, supersolids, and quantum liquids, within a single platform, as predicted by theories^{7,8,43,44}. Our results establish exciton geometry as a continuously tunable materials parameter, on par with density and temperature, enabling programmable excitonic materials and systematic exploration of interaction-driven quantum phase transitions in 2D bosonic systems.

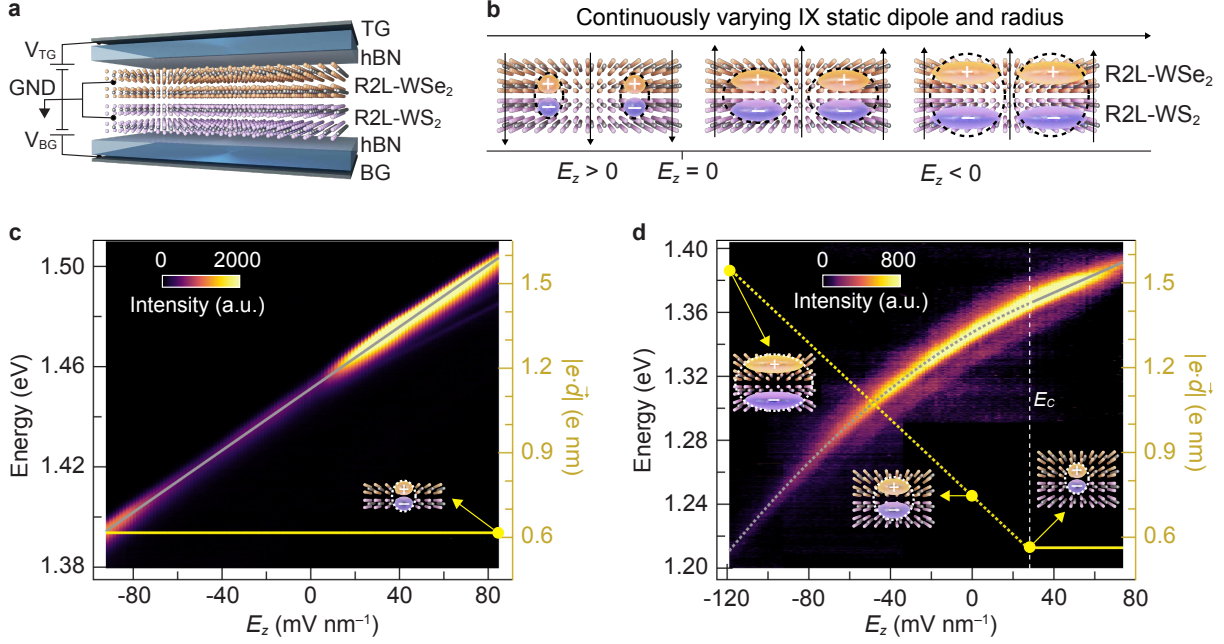


Fig. 1 | Interlayer exciton polarizability in a 2D hetero-tetralayer system. (a) Schematic of a dual-gate R2L-WSe₂/R2L-WS₂ device. Both top and bottom gates consist of few-layer graphite (3–5 layers); the gold contact to the TMD is bridged by a graphite flake. (b) Illustration of the continuously tunable interlayer exciton (IX) dipole moment under an out-of-plane electric field E_z (gray arrows). When E_z reaches a critical positive value (28 mV nm⁻¹), electrons and holes localize in the middle layers, forming a bilayer-limit dipolar IX. (c, d) E_z -dependent PL spectra of IXs in WSe₂/WS₂ (c) and in the hetero-tetralayer (d), measured at charge neutrality (Methods). Gray solid lines in (c) and (d) are linear Stark-shift fits; gray dashed curve in (d) is quadratic Stark-shift fit. The vertical white dashed line (~ 28 mV nm⁻¹) in (d) marks the field beyond which the tetralayer IX dipole moment reaches the bilayer limit, as schematically illustrated on either side. Yellow solid and dashed lines in (c) and (d) represent the first-order derivative of the E_z -dependent PL peak energy; particularly, yellow dashed line in (d) highlights the continuously tunable IX dipole moment ($e\vec{d}$) in the hetero-tetralayer structure. All spectra were acquired at 2 K with 500 nW continuous-wave (CW) excitation ($h\nu = 2.33$ eV).

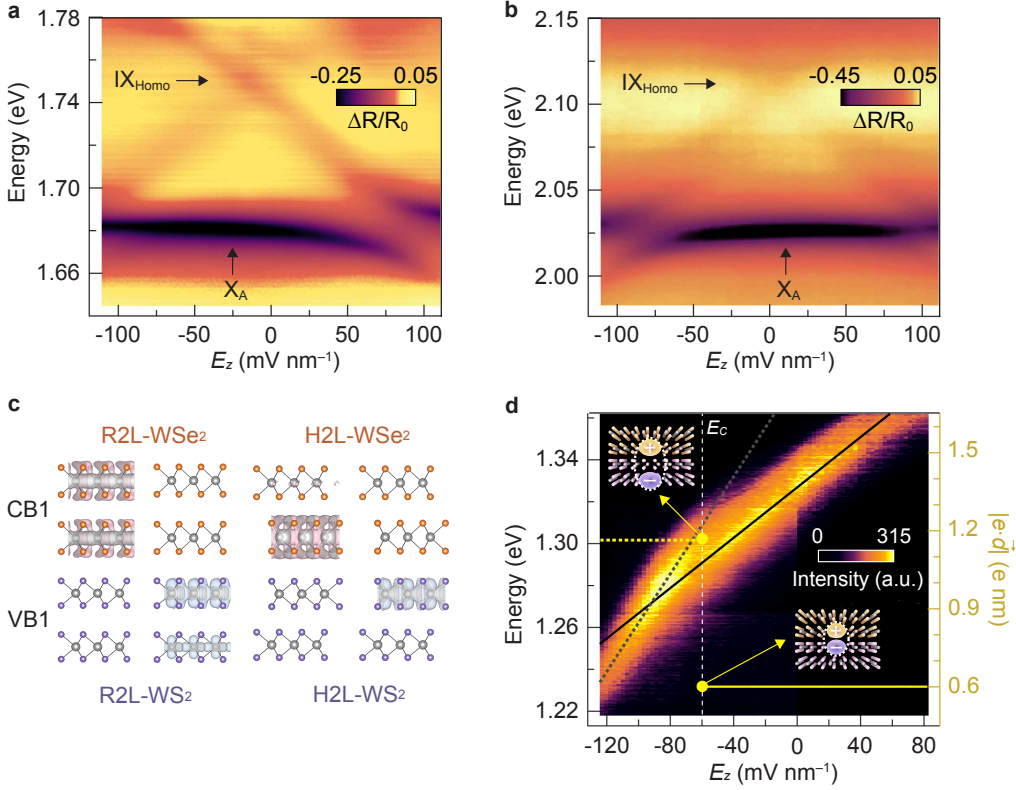


Fig. 2 | Interlayer hybridization in the hetero-tetrалayer system. **(a, b)** Reflectance contrast (RC) spectra versus out-of-plane electric field E_z for the WSe₂ **(a)** and WS₂ **(b)** A-exciton regimes in the R2L-WSe₂/R2L-WS₂ hetero-tetrалayer sample, measured at 2 K. **(c)** Spatial distributions of the electronic wavefunctions at the K -valley valence and conduction band edges for the R2L-WSe₂/R2L-WS₂ (left) and H2L-WSe₂/H2L-WS₂ (right) stacks. The corresponding DFT-calculated band dispersions are shown in Fig. S7. **(d)** E_z -dependent PL spectra of IXs in H2L-WSe₂/H2L-WS₂, acquired with 1 μ W CW excitation at 2 K ($h\nu = 2.33$ eV). Solid and dashed black lines in **(d)** are linear Stark shift fits, highlighting two distinct responses corresponding to IX dipole moments of 1.16 e nm (yellow dashed line) and 0.60 e nm (yellow solid line).

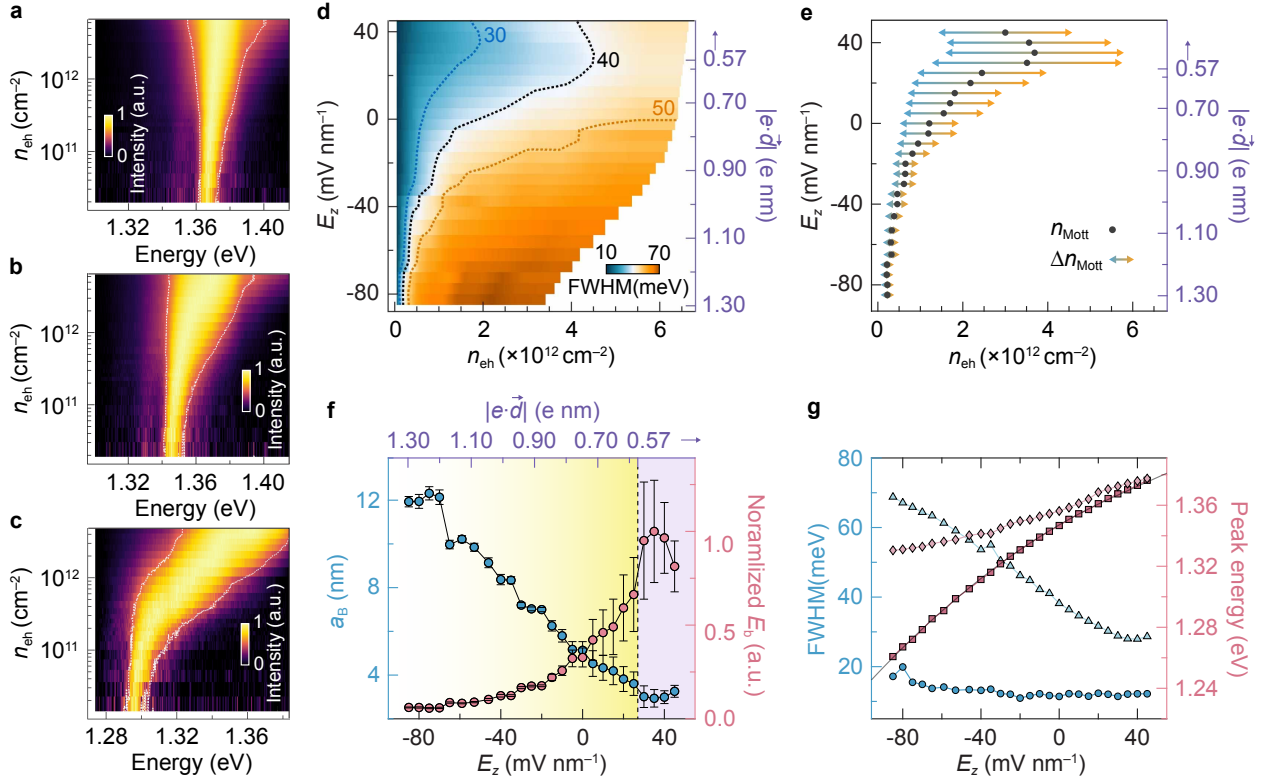


Fig. 3 | Field control of IX radius and geometry-driven gradual-to-abrupt Mott crossover. (a-c) Excitation-density (n_{eh})-dependent PL spectra of IXs in the R2L-WSe₂/R2L-WS₂ sample, acquired under out-of-plane electric fields $E_z = 30$ (a), 0 (b), and -53 (c) mV nm⁻¹. The excitation density spans 1.2×10^{10} cm⁻² to 6.8×10^{12} cm⁻². **(d)** FWHM map plotted versus E_z and n_{eh} for the same sample. The right axis shows the corresponding dipole moment $|e\vec{d}|$; for $E_z > 28$ mV nm⁻¹, $|e\vec{d}|$ saturates at 0.57 e nm (purple arrow). Dashed contours mark constant FWHM values of 30 (blue), 40 (black), and 50 (orange) meV. **(e)** Mott transition density range Δn_{eh} (blue-orange double arrows) at different electric field E_z . The black solid circles mark n_{Mott} . Δn_{eh} is obtained from logistic fitting of the n_{eh} -dependent FWHM (SI Text). **(f)** Estimated in-plane Bohr radius (a_B , purple) and binding energy (E_b , orange) of IXs in R2L-WSe₂/R2L-WS₂ as functions of out-of-plane electric field E_z (bottom axis) and corresponding dipole moment $|e\vec{d}|$ (top axis). Error bars denote uncertainty from the fitted Mott density. The black dashed line marks the field beyond which the tetralayer IX dipole moment reaches the bilayer limit. **(g)** E_z -dependent PL FWHM (blue symbols) and peak energy (red symbols) measured at fixed excitation densities. Dark blue circles and dark red squares correspond to $n_{eh} = 4.5 \times 10^{10}$ cm⁻²; light blue triangles and light red diamonds correspond to 1.5×10^{12} cm⁻²; the black solid curve represents the Stark-shift trajectory extracted from **Fig. 1d**.

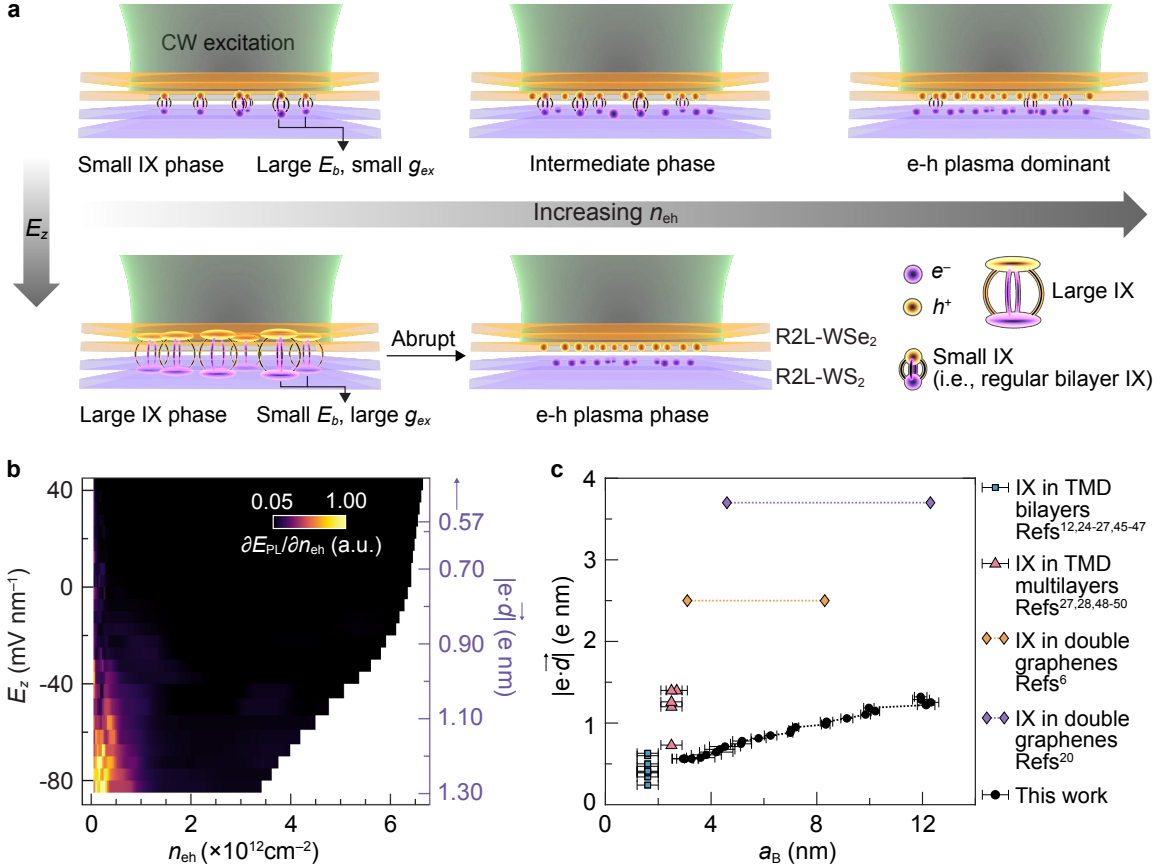


Fig. 4 | Excitonic interactions and the tunable IX geometry. (a) Schematic illustration of the electric-field-induced modulation of the IX geometry in the tetralayer and the resultant varying nature of IX-IX interactions. Increasing E_z redistributes the layer-hybridized electron and hole wavefunctions, enhancing the IX dipole moment $|e\vec{d}|$ and expanding the in-plane Bohr radius a_B . Tightly bound, small-size IXs display a softened interaction strength with increasing density, whereas the weakly bound large-size IXs exhibit an abrupt response to increasing density. (b) Optical stiffness map ($\partial E_{PL}/\partial n_{eh}$) plotted versus E_z and n_{eh} , where E_{PL} is the PL peak energy. The right-hand axis in (b) denotes IX dipole moment. Increasing E_z increases both the IX size and the optical stiffness, revealing possible cooperative tuning of exciton binding and exchange-driven IX-IX interactions. (c) Comparison of IX dipole moment and in-plane radius across previously reported IX systems (TMD bilayers, multilayers, and double-graphene heterostructures) and the present hetero-tetralayer platform. Blue squares denote IXs formed between adjacent layers^{12,24-27,45-47}. Red triangles represent IXs extending across multiple layers^{27,28,48-50}. a_B is extracted following the model in Ref⁸. The orange and purple diamonds label IXs in double-graphene structures separated by thin hBN spacers^{6,20}; horizontal dotted lines indicate the experimentally tunable a_B range via magnetic field. Black circles show our R2L-WSe₂/R2L-WS₂ results: the hetero-tetralayer platform uniquely provides simultaneous, continuous, and broad-range tunability of both $|e\vec{d}|$ and a_B .

Methods

Device fabrication

All 2D heterostructure samples were fabricated using a layer-by-layer van der Waals stacking technique. Monolayers of WSe₂ and WS₂ (HQ Graphene) were mechanically exfoliated from bulk crystals. Hexagonal boron nitride (hBN) flakes with thicknesses of 20-50 nm and atomically flat surfaces were also obtained by mechanical exfoliations. All flakes (WSe₂, WS₂, and hBN) were characterized by AFM and/or Raman spectroscopy prior to their use in device fabrications. A general stacking protocol is described in the following. A transparent polydimethylsiloxane (PDMS) stamp coated with a thin layer of polycarbonate (PC) was employed to sequentially pick up the following layers: top hBN flake, few-layer graphene top gate, top hBN encapsulation flake, graphite contact, TMD layers, bottom hBN encapsulation flake, few-layer graphene bottom gate, and bottom hBN flake. For preparing the R2L-WSe₂/R2L-WS₂ heterostructure, relatively large-area WSe₂ and WS₂ parental flakes were selected and then divided into two separate pieces by AFM cutting. Then, the resulting R2L-WSe₂ and R2L-WS₂ pieces could be subsequently stacked with high twist-angle accuracy. The completed heterostructure was transferred onto a clean silicon wafer with a 285-nm SiO₂ layer to provide optimal optical contrast, using an elevated transfer temperature of ~170-180 °C. Residual PC was removed with successive rinses of chloroform, acetone, and isopropanol. Metal-electrode patterns for connecting the graphite gates and contacts were defined by electron-beam lithography (FEI Helios 600 NanoLab) and reactive ion etching (PlasmaTherm Vision 320), followed by metal deposition of 5-nm Cr/100-nm Au (Angstrom electron-beam evaporation system).

Optical measurements

All optical measurements were performed using a home-built confocal microscope system (**Fig. S17**) integrated with a helium-recirculating optical cryostat (Quantum Design OptiCool, base temperature ~2 K) and a 100×, NA = 0.75 objective (Zeiss LD EC Epiplan-Neofluar 100×/0.75 DIC M27). Unless otherwise specified, device samples were maintained at ~2 K under vacuum during all experiments. A XYZ nanopositioner (Attocube) was used to position the sample, and a scanning Galvo system (Thorlabs GVS012) within the confocal setup enabled precise control over the excitation and signal-collection area. Continuous-wave (CW) excitation was provided by a 532 nm laser diode (Thorlabs DJ532-40). For time-resolved measurements, excitation was achieved with a 730 nm pulsed laser (Light Conversion ORPHEUS-N-2H, pumped by PHAROS PH2-10W, 250 kHz). A stabilized tungsten-halogen lamp (Thorlabs SLS201L) served as the broadband white-light source for reflectance spectroscopy. With the cryostat objective, laser beams were focused to a ~1 μm spot size, while lamp light was collimated and reshaped to achieve a diffraction-limited spot size (~1 μm). Steady-state PL and reflectance signals were collected and spectrally resolved using a spectrograph (Princeton Instruments HRS-500) equipped with a 600 g/mm diffraction

grating and detected with a cryogenically cooled InGaAs array camera (Princeton Instruments PyLoN-IR). Time-resolved PL was measured by time-correlated single-photon counting, using a single-photon counting module (Excelitas SPCM-AQRH) synchronized with the pulsed laser and recorded with a time-tagging electronics module (PicoQuant TimeHarp 260).

Electric field control

The equivalent circuit of our dual-gate device was a parallel plate capacitor with a 2D sheet of material (i.e., the TMDC heterostructure) in the middle. The dielectric constants for h-BN and TMDC are $\epsilon_{h-BN} \approx 3.9$, and $\epsilon_{TMDC} \approx 7.2^{12,15}$. Then, the electric field generated in between the top and bottom gates can be expressed as $E_z = \frac{V_{tg} - V_{bg}}{d_{hBN}} \cdot \frac{\epsilon_{h-BN}}{\epsilon_{TMDC}}$, where V_{tg} and V_{bg} are the top and bottom gate voltages, respectively; d_{hBN} is the total thickness of top and bottom hBN. Prior to scanning E_z , we performed a gate-gate reflectance map, to better identify the ratio of V_{tg}/V_{bg} that ensures a pure E_z without doping effect (**Fig. S2**). Gate voltages were supplied via two identical source meters (Keithley 2450, source accuracy $\sim 0.012\%$, calibrated) which were computer controlled through a GPIB bus.

DFT calculations

Spin-orbit-coupled density functional theory (DFT+SOC) calculations were carried out using the plane-wave code Quantum Espresso⁵¹⁻⁵³. We used the Perdew–Burke–Ernzerhof (PBE) functional of the generalized-gradient approximation (GGA)⁵⁴ as the exchange-correlation energy. Core–valence interactions were treated by full relativistic projector-augmented-wave (PAW) pseudopotentials⁵⁵. A kinetic energy cutoff of 100 Ry was applied to the wavefunctions. The two-dimensional heterostructures were modeled with an in-plane lattice constant of $a = 3.19$ Å and a vacuum spacing of at least 20 Å along the out-of-plane direction to suppress interlayer interactions between image atoms. $14 \times 14 \times 1$ k -mesh is employed in the first Brillouin-zone integrations. Electronic self-consistent calculation was converged to 1×10^{-10} Ry in total energy, and atomic positions were relaxed until the residual forces on all atoms were below 1×10^{-3} Ry/Bohr. Long-range dispersion interactions were included via the DFT-D3 correction⁵⁶.

Data availability

The data that support the findings of this study are presented in the article and its Supplementary Information. Further data are available from the corresponding author upon request.

References:

- (1) Koch, S. W.; Kira, M.; Khitrova, G. & Gibbs, H. M. Semiconductor excitons in new light. *Nat. Mater.* **5**, 523-531 (2006).
- (2) Wang, G.; Chernikov, A.; Glazov, M. M.; Heinz, T. F.; Marie, X.; Amand, T. & Urbaszek, B. *Colloquium*: Excitons in atomically thin transition metal dichalcogenides. *Rev. Mod. Phys.* **90**, 021001 (2018).
- (3) Ciarrocchi, A.; Tagarelli, F.; Avsar, A. & Kis, A. Excitonic devices with van der Waals heterostructures: valleytronics meets twistronics. *Nat. Rev. Mater.* **7**, 449-464 (2022).
- (4) Wang, Z. F.; Rhodes, D. A.; Watanabe, K.; Taniguchi, T.; Hone, J. C.; Shan, J. & Mak, K. F. Evidence of high-temperature exciton condensation in two-dimensional atomic double layers. *Nature* **574**, 76-80 (2019).
- (5) Xiong, R. C.; Nie, J. H.; Brantly, S. L.; Hays, P.; Sailus, R.; Watanabe, K.; Taniguchi, T.; Tongay, S. & Jin, C. H. Correlated insulator of excitons in WSe₂/WS₂ moiré superlattices. *Science* **380**, 860-864 (2023).
- (6) Liu, X. M.; Li, J. I. A.; Watanabe, K.; Taniguchi, T.; Hone, J.; Halperin, B.; Kim, P. & Dean, C. R. Crossover between strongly coupled and weakly coupled exciton superfluids. *Science* **375**, 205-209 (2022).
- (7) Conti, S.; Perali, A.; Hamilton, A. R.; Milosevic, M. V.; Peeters, F. M. & Neilson, D. Chester supersolid of spatially indirect excitons in double-layer semiconductor heterostructures. *Phys. Rev. Lett.* **130**, 057001 (2023).
- (8) Fogler, M. M.; Butov, L. V. & Novoselov, K. S. High-temperature superfluidity with indirect excitons in van der Waals heterostructures. *Nat. Commun.* **5**, 4555 (2014).
- (9) Randeria, M. & Taylor, E. Crossover from Bardeen-Cooper-Schrieffer to Bose-Einstein condensation and the unitary Fermi gas. *Annu. Rev. Condens. Matter Phys.* **5**, 209-232 (2014).
- (10) Deng, S. B.; Park, H.; Reimann, J.; Peterson, J. M.; Blach, D. D.; Sun, M. J.; Yan, T. F.; Sun, D. W.; Taniguchi, T.; Watanabe, K.; Xu, X. D.; Kennes, D. M. & Huang, L. B. Frozen non-equilibrium dynamics of exciton Mott insulators in moiré superlattices. *Nat. Mater.* **24**, 527–534 (2025).
- (11) Wang, J.; Ardelean, J.; Bai, Y. S.; Steinhoff, A.; Florian, M.; Jahnke, F.; Xu, X. D.; Kira, M.; Hone, J. & Zhu, X. Y. Optical generation of high carrier densities in 2D semiconductor heterobilayers. *Sci. Adv.* **5**, eaax0145 (2019).
- (12) Jauregui, L. A.; Joe, A. Y.; Pistunova, K.; Wild, D. S.; High, A. A.; Zhou, Y.; Scuri, G.; De Greve, K.; Sushko, A.; Yu, C. H.; Taniguchi, T.; Watanabe, K.; Needleman, D. J.; Lukin, M. D.; Park, H. & Kim, P. Electrical control of interlayer exciton dynamics in atomically thin heterostructures. *Science* **366**, 870-875 (2019).

(13) Huang, S. Y.; Yu, B. Y.; Ma, Y. X.; Pan, C. H.; Ma, J. W.; Zhou, Y. X.; Ma, Y. Z. H.; Yang, K.; Wu, H.; Lei, Y. C.; Xing, Q. X.; Mu, L.; Zhang, J. S.; Mou, Y. L. & Yan, H. G. Bright dipolar excitons in twisted black phosphorus homostructures. *Science* **386**, 526-531 (2024).

(14) Li, W. J.; Hadjri, Z.; Devenica, L. M.; Zhang, J.; Liu, S.; Hone, J.; Watanabe, K.; Taniguchi, T.; Rubio, A. & Srivastava, A. Quadrupolar-dipolar excitonic transition in a tunnel-coupled van der Waals heterotrilayer. *Nat. Mater.* **22**, 1478-1484 (2023).

(15) Yu, L.; Pistunova, K.; Hu, J. Y.; Watanabe, K.; Taniguchi, T. & Heinz, T. F. Observation of quadrupolar and dipolar excitons in a semiconductor heterotrilayer. *Nat. Mater.* **22**, 1485-1491 (2023).

(16) Xie, Y. Z.; Gao, Y. C.; Chen, F. Y.; Wang, Y. K.; Mao, J.; Liu, Q. Y.; Chu, S. S.; Yang, H.; Ye, Y.; Gong, Q. H.; Feng, J. & Gao, Y. A. Bright and dark quadrupolar excitons in the WSe₂/MoSe₂/WSe₂ heterotrilayer. *Phys. Rev. Lett.* **131**, 186901 (2023).

(17) Lian, Z.; Chen, D. X.; Ma, L.; Meng, Y. Z.; Su, Y.; Yan, L.; Huang, X.; Wu, Q. R.; Chen, X. Y.; Blei, M.; Taniguchi, T.; Watanabe, K.; Tongay, S.; Zhang, C. W.; Cui, Y. T. & Shi, S. F. Quadrupolar excitons and hybridized interlayer Mott insulator in a trilayer moiré superlattice. *Nat. Commun.* **14**, 4604 (2023).

(18) Bai, Y. S.; Li, Y. L.; Liu, S.; Guo, Y. J.; Pack, J.; Wang, J.; Dean, C. R.; Hone, J. & Zhu, X. Y. Evidence for exciton crystals in a 2D semiconductor heterotrilayer. *Nano Lett.* **23**, 11621-11629 (2023).

(19) Meng, Y. Z.; Ma, L.; Yan, L.; Khalifa, A.; Chen, D. X.; Zhang, S.; Banerjee, R.; Taniguchi, T.; Watanabe, K.; Tongay, S. A.; Hunt, B.; Lin, S. Z.; Yao, W.; Cui, Y. T.; Chatterjee, S. & Shi, S. F. Strong-interaction-driven quadrupolar-to-dipolar exciton transitions in a trilayer moiré superlattice. *Nat. Photon.* **19**, 1219–1224 (2025).

(20) Li, J. I. A.; Taniguchi, T.; Watanabe, K.; Hone, J. & Dean, C. R. Excitonic superfluid phase in double bilayer graphene. *Nat. Phys.* **13**, 751-755 (2017).

(21) Wang, F.; Shan, J.; Islam, M. A.; Herman, I. P.; Bonn, M. & Heinz, T. F. Exciton polarizability in semiconductor nanocrystals. *Nat. Mater.* **5**, 861-864 (2006).

(22) Lei, Y. C.; Ma, J. W.; Luo, J. M.; Huang, S. Y.; Yu, B. Y.; Song, C. Y.; Xing, Q. X.; Wang, F. J.; Xie, Y. A.; Zhang, J. S.; Mu, L.; Ma, Y. X.; Wang, C. & Yan, H. G. Layer-dependent exciton polarizability and the brightening of dark excitons in few-layer black phosphorus. *Nat. Commun.* **14**, 5314 (2023).

(23) Roch, J. G.; Leisgang, N.; Froehlicher, G.; Makk, P.; Watanabe, K.; Taniguchi, T.; Schonenberger, C. & Warburton, R. J. Quantum-confined stark effect in a MoS₂ monolayer van der Waals heterostructure. *Nano Lett.* **18**, 1070-1074 (2018).

(24) Ciarrocchi, A.; Unuchek, D.; Avsar, A.; Watanabe, K.; Taniguchi, T. & Kis, A. Polarization switching and electrical control of interlayer excitons in two-dimensional van der Waals heterostructures. *Nat. Photon.* **13**, 131-136 (2019).

(25) Leisgang, N.; Shree, S.; Paradisanos, I.; Sponfeldner, L.; Robert, C.; Lagarde, D.; Balocchi, A.; Watanabe, K.; Taniguchi, T.; Marie, X.; Warburton, R. J.; Gerber, I. C. & Urbaszek, B. Giant Stark splitting of an exciton in bilayer MoS₂. *Nat. Nanotechnol.* **15**, 901-907 (2020).

(26) Sung, J.; Zhou, Y.; Scuri, G.; Zólyomi, V.; Andersen, T. I.; Yoo, H.; Wild, D. S.; Joe, A. Y.; Gelly, R. J.; Heo, H.; Magorrian, S. J.; Bérubé, D.; Valdivia, A. M. M.; Taniguchi, T.; Watanabe, K.; Lukin, M. D.; Kim, P.; Fal'ko, V. I. & Park, H. Broken mirror symmetry in excitonic response of reconstructed domains in twisted MoSe₂/MoSe₂ bilayers. *Nat. Nanotechnol.* **15**, 750-754 (2020).

(27) Feng, S.; Campbell, A. J.; Brotons-Gisbert, M.; Andres-Penares, D.; Baek, H.; Taniguchi, T.; Watanabe, K.; Urbaszek, B.; Gerber, I. C. & Gerardot, B. D. Highly tunable ground and excited state excitonic dipoles in multilayer 2H-MoSe₂. *Nat. Commun.* **15**, 4377 (2024).

(28) Zhang, Y. N.; Xiao, C. X.; Ovchinnikov, D.; Zhu, J. Y.; Wang, X.; Taniguchi, T.; Watanabe, K.; Yan, J. Q.; Yao, W. & Xu, X. D. Every-other-layer dipolar excitons in a spin-valley locked superlattice. *Nat. Nanotechnol.* **18**, 501-506 (2023).

(29) Tang, Y. H.; Gu, J.; Liu, S.; Watanabe, K.; Taniguchi, T.; Hone, J.; Mak, K. F. & Shan, J. Tuning layer-hybridized moiré excitons by the quantum-confined Stark effect. *Nat. Nanotechnol.* **16**, 52-57 (2021).

(30) Liu, X. L.; Leisgang, N.; Dolgirev, P. E.; Zibrov, A. A.; Sung, J.; Wang, J.; Taniguchi, T.; Watanabe, K.; Walther, V.; Park, H.; Demler, E.; Kim, P. & Lukin, M. D. Optical signatures of interlayer electron coherence in a bilayer semiconductor. *Nat. Phys.* **21**, 1563–1569 (2025).

(31) Hsu, W. T.; Lin, B. H.; Lu, L. S.; Lee, M. H.; Chu, M. W.; Li, L. J.; Yao, W.; Chang, W. H. & Shih, C. K. Tailoring excitonic states of van der Waals bilayers through stacking configuration, band alignment, and valley spin. *Sci. Adv.* **5**, eaax7407 (2019).

(32) Stern, M.; Garmider, V.; Umansky, V. & Bar-Joseph, I. Mott transition of excitons in coupled quantum wells. *Phys. Rev. Lett.* **100**, 256402 (2008).

(33) Joe, A. Y.; Valdivia, A. M. M.; Jauregui, L. A.; Pistunova, K.; Ding, D. P.; Zhou, Y.; Scuri, G.; De Greve, K.; Sushko, A.; Kim, B.; Taniguchi, T.; Watanabe, K.; Hone, J. C.; Lukin, M. D.; Park, H. & Kim, P. Controlled interlayer exciton ionization in an electrostatic trap in atomically thin heterostructures. *Nat. Commun.* **15**, 6743 (2024).

(34) Klingshirn, C. & Haug, H. Optical-properties of highly excited direct gap semiconductors. *Phys. Rep.* **70**, 315-398 (1981).

(35) Kappei, L.; Szczytko, J.; Morier-Genoud, F. & Deveaud, B. Direct observation of the Mott transition in an optically excited semiconductor quantum well. *Phys. Rev. Lett.* **94**, 147403 (2005).

(36) Chernikov, A.; Ruppert, C.; Hill, H. M.; Rigosi, A. F. & Heinz, T. F. Population inversion and giant bandgap renormalization in atomically thin WS₂ layers. *Nat. Photon.* **9**, 466-470 (2015).

(37) Dendzik, M.; Xian, R. P.; Perfetto, E.; Sangalli, D.; Kutnyakhov, D.; Dong, S.; Beaulieu, S.; Pincelli, T.; Pressacco, F.; Curcio, D.; Agustsson, S. Y.; Heber, M.; Hauer, J.; Wurth, W.; Brenner, G.; Acremann, Y.; Hofmann, P.; Wolf, M.; Marini, A.; Stefanucci, G.; Rettig, L. & Ernststorfer, R. Observation of an excitonic Mott transition through ultrafast core-cum-conduction photoemission spectroscopy. *Phys. Rev. Lett.* **125**, 096401 (2020).

(38) Bataller, A. W.; Younts, R. A.; Rustagi, A.; Yu, Y. L.; Ardekani, H.; Kemper, A.; Cao, L. Y. & Gundogdu, K. Dense electron-hole plasma formation and ultralong charge lifetime in monolayer MoS₂ via material tuning. *Nano Lett.* **19**, 1104-1111 (2019).

(39) Guerci, D.; Capone, M. & Fabrizio, M. Exciton Mott transition revisited. *Phys. Rev. Mater.* **3**, 054605 (2019).

(40) Laikhtman, B. & Rapaport, R. Exciton correlations in coupled quantum wells and their luminescence blue shift. *Phys. Rev. B* **80**, 195313 (2009).

(41) Schindler, C. & Zimmermann, R. Analysis of the exciton-exciton interaction in semiconductor quantum wells. *Phys. Rev. B* **78**, 045313 (2008).

(42) Erkensten, D.; Brem, S. & Malic, E. Exciton-exciton interaction in transition metal dichalcogenide monolayers and van der Waals heterostructures. *Phys. Rev. B* **103**, 045426 (2021).

(43) Dai, D. D. & Fu, L. Strong-coupling phases of trions and excitons in electron-hole bilayers at commensurate densities. *Phys. Rev. Lett.* **132**, 196202 (2024).

(44) Vu, D. & Das Sarma, S. Excitonic phases in a spatially separated electron-hole ladder model. *Phys. Rev. B* **108**, 235158 (2023).

(45) Karni, O.; Barré, E.; Lau, S. C.; Gillen, R.; Ma, E. Y.; Kim, B.; Watanabe, K.; Taniguchi, T.; Maultzsch, J.; Barmak, K.; Page, R. H. & Heinz, T. F. Infrared interlayer exciton emission in MoS₂/WSe₂ heterostructures. *Phys. Rev. Lett.* **123**, 247402 (2019).

(46) Peimyoo, N.; Deilmann, T.; Withers, F.; Escolar, J.; Nutting, D.; Taniguchi, T.; Watanabe, K.; Taghizadeh, A.; Craciun, M. F.; Thygesen, K. S. & Russo, S. Electrical tuning of optically active interlayer excitons in bilayer MoS₂. *Nat. Nanotechnol.* **16**, 888-893 (2021).

(47) Tagarelli, F.; Lopriore, E.; Erkensten, D.; Perea-Causín, R.; Brem, S.; Hagel, J.; Sun, Z.; Pasquale, G.; Watanabe, K.; Taniguchi, T.; Malic, E. & Kis, A. Electrical control of hybrid exciton transport in a van der Waals heterostructure. *Nat. Photon.* **17**, 615-621 (2023).

(48) Mahdikhanyarvejahan, F.; Shanks, D. N.; Klein, M.; Wang, Q.; Koehler, M. R.; Mandrus, D. G.; Taniguchi, T.; Watanabe, K.; Monti, O. L. A.; LeRoy, B. J. & Schaibley, J. R. Localized interlayer excitons in MoSe₂-WSe₂ heterostructures without a moiré potential. *Nat. Commun.* **13**, 5354 (2022).

(49) Shanks, D. N.; Mahdikhanyarvejahan, F.; Koehler, M. R.; Mandrus, D. G.; Taniguchi, T.; Watanabe, K.; LeRoy, B. J. & Schaibley, J. R. Single-exciton trapping in an electrostatically defined two-dimensional semiconductor quantum dot. *Phys. Rev. B* **106**, L201401 (2022).

(50) Lian, Z.; Chen, D. X.; Meng, Y. Z.; Chen, X. T.; Su, Y.; Banerjee, R.; Taniguchi, T.; Watanabe, K.; Tongay, S.; Zhang, C. W.; Cui, Y. T. & Shi, S. F. Exciton superposition across moiré states in a semiconducting moiré superlattice. *Nat. Commun.* **14**, 5042 (2023).

(51) Giannozzi, P.; Andreussi, O.; Brumme, T.; Bunau, O.; Nardelli, M. B.; Calandra, M.; Car, R.; Cavazzoni, C.; Ceresoli, D.; Cococcioni, M.; Colonna, N.; Carnimeo, I.; Dal Corso, A.; de Gironcoli, S.; Delugas, P.; DiStasio, R. A.; Ferretti, A.; Floris, A.; Fratesi, G.; Fugallo, G.; Gebauer, R.; Gerstmann, U.; Giustino, F.; Gorni, T.; Jia, J.; Kawamura, M.; Ko, H. Y.; Kokalj, A.; Küçükbenli, E.; Lazzeri, M.; Marsili, M.; Marzari, N.; Mauri, F.; Nguyen, N. L.; Nguyen, H. V.; Otero-de-la-Roza, A.; Paulatto, L.; Poncé, S.; Rocca, D.; Sabatini, R.; Santra, B.; Schlipf, M.; Seitsonen, A. P.; Smogunov, A.; Timrov, I.; Thonhauser, T.; Umari, P.; Vast, N.; Wu, X. & Baroni, S. Advanced capabilities for materials modelling with QUANTUM ESPRESSO. *J. Phys. Condens. Matter* **29**, 465901 (2017).

(52) Giannozzi, P.; Baroni, S.; Bonini, N.; Calandra, M.; Car, R.; Cavazzoni, C.; Ceresoli, D.; Chiarotti, G. L.; Cococcioni, M.; Dabo, I.; Dal Corso, A.; de Gironcoli, S.; Fabris, S.; Fratesi, G.; Gebauer, R.; Gerstmann, U.; Gouguassis, C.; Kokalj, A.; Lazzeri, M.; Martin-Samos, L.; Marzari, N.; Mauri, F.; Mazzarello, R.; Paolini, S.; Pasquarello, A.; Paulatto, L.; Sbraccia, C.; Scandolo, S.; Sclauzero, G.; Seitsonen, A. P.; Smogunov, A.; Umari, P. & Wentzcovitch, R. M. QUANTUM ESPRESSO: a modular and open-source software project for quantum simulations of materials. *J. Phys. Condens. Matter* **21**, 395502 (2009).

(53) Giannozzi, P.; Baseggio, O.; Bonfà, P.; Brunato, D.; Car, R.; Carnimeo, I.; Cavazzoni, C.; de Gironcoli, S.; Delugas, P.; Ruffino, F. F.; Ferretti, A.; Marzari, N.; Timrov, I.; Urru, A. & Baroni, S. Quantum ESPRESSO toward the exascale. *J. Chem. Phys.* **152**, 154105 (2020).

(54) Perdew, J. P.; Burke, K. & Ernzerhof, M. Generalized gradient approximation made simple. *Phys. Rev. Lett.* **77**, 3865-3868 (1996).

(55) Blochl, P. E. Projector augmented-wave method. *Phys. Rev. B* **50**, 17953-17979 (1994).

(56) Grimme, S.; Antony, J.; Ehrlich, S. & Krieg, H. A consistent and accurate ab initio parametrization of density functional dispersion correction (DFT-D) for the 94 elements H-Pu. *J. Chem. Phys.* **132**, 154104 (2010).

Author contributions

Y.B. conceived the research and oversaw the project. Z.S. fabricated the devices and performed the optical experiments with assistance from Y.B., H.S., A.L., N.J.Z., K.S.H., J.D., C.Y.L., and J.W. X.J. and B.R. performed the theoretical calculations. K.W. and T.T. grew the hBN crystals. Y.B. and Z.S. analyzed the data with inputs from O.C., J.W., and J.L. All authors discussed the results and commented on the manuscript.

Competing interests: The authors declare no competing interests.

Data and materials availability: All data are available in the main text or the supplementary materials.